

Benchmarking cryo-EM single particle analysis workflow

Laura Y. Kim¹, William J. Rice¹, Edward T. Eng¹, Mykhailo Kopylov¹, Anchi Cheng¹, Ashleigh M. Raczowski¹, Kelsey D. Jordan¹, Daija Bobe¹, Clinton S. Potter^{1*} and Bridget Carragher^{1*}

¹ Simons Electron Microscopy Center, New York Structural Biology Center, New York, NY, USA

*** Correspondence:**

Bridget Carragher

bcarr@nysbc.org

Keywords: Cryo-electron microscopy, benchmarking, alignment, structural biology, single particle workflow, resolution

Abstract

Cryo electron microscopy facilities running multiple instruments and serving users with varying skill levels need a robust and reliable method for benchmarking both the hardware and software components of their single particle analysis workflow. The workflow is complex, with many bottlenecks existing at the specimen preparation, data collection and image analysis steps; the samples and grid preparation can be of unpredictable quality, there are many different protocols for microscope and camera settings, and there is a myriad of software programs for analysis that can depend on dozens of settings chosen by the user. For this reason, we believe it is important to benchmark the entire workflow, using a standard sample and standard operating procedures, on a regular basis. This provides confidence that all aspects of the pipeline are capable of producing maps to high resolution. Here we describe benchmarking procedures using a test sample, rabbit muscle aldolase.

1 Introduction

At the Simons Electron Microscopy Center (SEMC) at the New York Structural Biology Center (NYSBC) in New York, NY, our mission is to provide scientific expertise and resources for our users in their studies of biological macromolecules, with a focus on high-resolution structure determination. Our facility is home to seven electron microscopes (EMs), including three 300 kV FEI Titan Krios instruments, all of which are routinely checked for their performance using a series of benchmarking tests. While these checks include standard testing for performance and resolution, typically using a cross grating replica, we believe it is also important to test our systems using a biological sample that scrutinizes the entire workflow from specimen preparation through imaging and image processing. This benchmarking enables us not only to assess any limitations and bottlenecks that might arise, but also allows us to optimize the single particle analysis (SPA) workflow, thus maximizing the throughput and performance of instrumentation and data collection strategies. In addition to the practical advantages of benchmarking, the overall workflow serves as an educational tool for newcomers to cryo electron microscopy (cryo-EM) who wish to learn the SPA workflow using a protein that can be routinely reconstructed to high resolution. Finally, benchmarking tests provide an objective measure to the user that the instrumentation is operating at

its top optical efficiency, capable of providing good quality structures, and that any limitations to resolution are thus most likely related to an individual sample.

Benchmarking efforts for SPA are not straightforward for EM labs. This challenge is due in part to the lack of an "industry standard" biological EM specimen and also due to intrinsic variabilities that exist at the specimen purification and grid preparation level. This variability is then coupled with a wide range of data collection and image processing strategies and software choices. An ideal cryo-EM benchmarking standard would be a biological specimen with the following attributes: 1) easily accessible (i.e. commercially available and requiring minimal additional purification), 2) low maintenance sample preparation, 3) biochemically stable over a range of temperatures and time periods, 4) little to no conformational and compositional heterogeneity.

It is also important that the benchmark results in a structure with a sufficiently high resolution, which we consider to be below 3 Å, in order to give confidence in users as to the performance of the instrument, the data collection protocols and the processing pipeline. There are currently 36 unique structures in the EMDataBank at a sub 3 Å resolution that have been obtained by SPA. These include the 465 kD beta-galactosidase at 2.2 Å resolution (Bartesaghi et al. 2015), the 540 kD p97 at 2.3 Å (Banerjee et al. 2016), the 334 kD glutamate dehydrogenase at 1.8 Å (Merk et al. 2016) and the 150 kD aldolase at 2.6 Å (Herzik, Wu, and Lander 2017) as well as larger proteins that have been used as standards in cryo-EM SPA, like the 700 kDa *T. acidophilum* 20S proteasome (Li et al. 2013, Danev, Tegunov, and Baumeister 2017, Campbell et al. 2014, Campbell et al. 2015, Danev and Baumeister 2016) and 440 kDa apoferritin (Russo and Passmore 2014, Rickgauer, Grigorieff, and Denk 2017, Arnold et al. 2017).

In this paper, we present a workflow for single particle reconstruction using a robust and reliable benchmarking standard: rabbit muscle aldolase, a small homotetrameric glycolytic enzyme with a molecular weight of ~150 kDa. Our goal is to present this benchmarking procedure as a step-by-step workflow that can be readily repeated. We show that in order to achieve a sub 3 Å reconstruction of aldolase in a reasonable time frame, ice thickness of 10–20 nm is essential.

2 Methods and Materials

2.1 Sample Preparation

The sample was prepared as previously described with minor adjustments (Herzik, Wu, and Lander 2017). Briefly, pure aldolase isolated from rabbit muscle (Sigma Aldrich, product #A2714) was solubilized in 20 mM HEPES (pH 7.5), 50 mM NaCl at 3 mg/ml and further purified using a Superose 6 10/300 GL (GE Healthcare) column equilibrated in solubilization buffer. SDS-PAGE analysis was used to confirm sample purity of peak fractions, which were pooled and concentrated to 10 mg/mL and flash frozen in 10 µl aliquots for long term storage. The protein was diluted to 1.5 mg/ml final concentration for grid preparation. Vitrified specimens were prepared by adding 3 µl aldolase (1.5 mg/ml) to freshly plasma cleaned (Gatan Solarus plasma cleaner, 75% argon/25% oxygen atmosphere at 15 Watts for 6 seconds) Au R1.2/1.3 300-mesh (EMS UltrAuFoil®) grids. To minimize the effects of beam induced motion during acquisition, samples were prepared on gold grids (Russo and Passmore 2014). Grids were blotted for 1 s after a 10 s pre-blotting time, then plunge-frozen in liquid ethane using a Leica EM GP instrument (Leica Microsystems), with the chamber maintained at 4°C and 90% humidity.

2.2 Microscope Alignment

Complete microscope alignment procedure, based on the FEI on-line manual, were performed during installation using a cross-grating calibration grid (Titan on-line help manual—Alignments, version 2.6 and higher). A minimal subset of the alignments is performed before each daily data collection. These include dark and bright gain corrections and energy filter alignment, performed over vacuum, and beam tilt pivot points and Cs (spherical aberration coefficient) correction, performed at eucentric height and eucentric focus over carbon. Second-order axial coma free alignment and astigmatism minimization was done using the Cs corrector, aligning until A1 (2-fold astigmatism) was less than 10 nm and B2 (coma) was less than 50 nm. Re-tuning of the Cs corrector was performed if the CTF estimation indicated a differential between the major and minor axis of greater than 100 nm. A full tune of the energy filter was carried out daily and energy filter slit was realigned every 60 minutes, managed automatically by Leginon (Suloway et al. 2005). The image distortion after tuning is typically within 0.2 %, and the slit movement was generally +/- 1 eV. The goal of these alignments is to verify the presence of Thon rings visible beyond 3 Å resolution in the power spectrum of aligned images collected over amorphous carbon using the same imaging conditions as for the data collection. The eucentric height and eucentric focus are set using Leginon (Suloway et al. 2005) by minimizing movement caused by stage tilt. The beam intensity was kept well within the parallel range of the 3-condenser lens Titan system, with the illuminated beam diameter at least 2–3 times larger than the minimum required for parallel illumination. At a nominal magnification of 130,000x the calibrated beam diameter for parallel illumination is 0.45 – 12.0 µm. In general, the beam diameter was set to be slightly larger than the nominal hole size of 1.2 µm. This helps to ensure that the beam will contact the gold substrate during exposure collection, potentially helping to dissipate charge onto the substrate instead of the sample. Dose rate measurements on the Gatan K2 Summit direct electron detector (DED) were collected to determine whether or not changes to spot size were necessary to achieve the desired dose rate. All high magnification imaging was done in the nanoprobe mode with a 70 µm C2 aperture and a 100 µm objective aperture.

2.3 Data Collection

Table 1 summarizes the data collection statistics for three different datasets, 17sep21j, 17nov02c, and 17dec27a. Briefly, data was acquired using a Titan Krios with a spherical aberration corrector and a post-column Gatan Image Filter (GIF) operating in nanoprobe and EF-TEM mode with an extraction voltage of 4250 V, a gun lens setting of 4, a spot size of 6 or 7, a C2 aperture size of 70 µm, an objective aperture size of 100 µm, and an energy filter slit width of 20 eV. The microscope is equipped with a field emission gun operating in the X-FEG module. Data was collected automatically using the *MSI-T2* application in Leginon and all image pre-processing was performed using the Appion pipeline (Lander et al. 2009). Square and sub-square level images were targeted by stage position movement, with a 2 and 5 second pause before imaging, respectively. Drift monitor cutoff was 6 Å/sec. Focusing was performed on the gold substrate, after which four final high-magnification movies were acquired by image shift targeting with a 5 second pause before the first image and 2.5 second pause before each subsequent movie. Final high-magnification movies were taken at a nominal magnification of 130,000x (calibrated pixel size of 0.855 Å at the detector level) and a nominal defocus range of -1.0 to -2.0 µm defocus with the Gatan K2 Summit DED operating in either counting or super-resolution mode. Each movie was acquired over 6000–6600 ms with a frame rate of 5 frames/sec and a dose rate of 8 electrons/pixel/sec. The total cumulative dose for all datasets was in the range of 60–70 electrons/Å².

In addition to our standard data collection workflow, we routinely collect ice thickness measurements for each high magnification movie. This is done by comparing the intensities of images taken without and with the energy filter slit inserted (Rice et al. 2018) (Figure 1D, 1H and 1L).

2.4 Concurrent Image Processing

During data collection, images were pre-processed to provide a feedback on image quality. All pre-processing was carried out using the Appion pipeline (Lander et al. 2009). Mechanical and beam-induced motion correction and dose weighting were performed on the raw movies using MotionCor2 (Zheng et al. 2017) using a 5×5 patch size and a B-factor of 100 with 7 iterations. Super-resolution movies were binned by two before frame summation. Whole-image contrast transfer function (CTF) estimation was performed using CTFFind4 (Rohou and Grigorieff 2015). Particle picking was performed within Appion using FindEM template picking (Roseman 2004) with templates generated from images of the same sample acquired on a screening microscope. Box files from the particle picks were generated within Appion and exported for further processing. Subsets were exported for processing during collection and the final full datasets were then processed post-collection.

2.5 Post Collection Image Processing

Reference-free 2D classification was performed using cryoSPARC (Punjani et al. 2017) on particles binned by 4 with a box size of 256 pixels. Particles exhibiting secondary structure elements were selected for further processing, including initial model generation, and subsequent 3D classification and 3D auto-refinement using both RELION 2.0 (Kimanius et al. 2016) and cryoSPARC (Punjani et al. 2017). Default processing parameters were generally used. All reported resolutions are based on the 0.143 Fourier shell criterion (Henderson et al. 2012, Scheres and Chen 2012) with all Fourier shell correlation (FSC) curves corrected for the effects of soft- masking by high-resolution noise substitution (Chen et al. 2013). Data processing statistics, including number of particles and average processing times, are described in Table 2.

Figure 1 shows exemplary images from the datasets #1, #2, and #3. Figure 2 shows processing results from dataset #1 and #2, including 2D class averages, Euler plots, FSC curves, 3D maps, and ice thickness plots.

3 Results and Discussion

We describe three unique data sets that were processed based on three different sorting criteria: the first few hundred images collected for the session, all images collected in the session, images sorted by ice thickness < 25 nm, for a total of nine experiments (Table 2). The details of data acquisition and processing are provided in Table 1 and 2, respectively.

While all three data sets result in 3 Å or better maps, the major variable in terms of data and map quality was ice thickness. For grids with very thin ice, sub 3 Å maps can be obtained in a much shorter time period and with fewer images than from grids with much larger ice thickness. Use of image shift navigation as opposed to stage position navigation is our preferred mode of data collection as it helps to maximize acquisition throughput, and moderate amounts of image shift do not affect results at the targeted resolution (Cheng et al. 2018).

From experience (and personal communication with the Lander lab) we have concluded that it is very important to maximize the number of particles packed into each hole, while avoiding particle overlap and aggregation. This close packing provides a more accurate CTF estimation of each image since the protein contributes a high signal to the power spectrum of the image. We also hypothesize that the densely packed protein is instrumental in achieving a very thin ice layer, as it may help to retain a thin layer of liquid across the hole. Dense packing of the protein is concentration dependent and can lead to multiple layers of particles (Noble et al. 2017). This is refractory to high-resolution goals as

two layers of protein result in a whole-image defocus estimation averaged between the two layers, thus limiting the resolution of each particle depending on their distance from the midway point.

Table 2 shows the results of processing the 17sep21j dataset (#1, #1a and #1b) in three different ways including all 699 images (dataset #1), sorting based on including only images with < 25 nm ice thickness (dataset #1a) and using only the first 500 images (dataset #1b). We found that resolution of 2.5 Å can be achieved either by using all images or by using only those from the thinnest ice. Micrographs coming from the thinnest ice yield a higher resolution final reconstruction and thus limiting image acquisition to areas of thin ice is clearly a more efficient strategy than brute force processing of the largest number of images. The 17sep21j dataset is near-perfect in that it can yield a sub 3 Å reconstruction in under 24 hours, regardless of how the data is sorted because of the majority of images coming from a very thin ice.

The 17nov02c (#2, #2a and #2b) dataset is representative of the type of data collection that should be avoided if possible. This dataset required a large block of microscope time (52 hours), processing time and computational resources (over 1.3M particles before 2D classification). While dataset #2 yielded a 3.0 Å map it required a total data collection and processing duration of ~60 hours. Ideally, a benchmarking test should be accomplished in less than 24 hours. Also, the sorted data from this dataset (#2a and #2b) both provided reconstructions worse than 3.0 Å, due to the very small number of particles that are in thin ice.

The 17dec27a (#3) dataset yielded a similarly high-resolution data as the 17sep21j (#1) dataset, but it required more than twice the length of microscope and processing time, 49 hours versus 21 hours. Both datasets contributed about 200K particles to the final refinement, but 17dec27a (#3) started with more than twice the number of micrographs compared to 17sep21j (#1) (1614 versus 699 micrographs).

Table 3 ranks the datasets by nominal resolution. We find that all sub 3 Å reconstructions are derived from datasets with an ice thickness range of 10–20 nm, independent of how the data was sorted indicating that ice thickness is a primary driver of data quality for the SPA of aldolase. Quantitative metrics like ice thickness measurements, or qualitative metrics such as the presence of an ice ring in the power spectrum of the image should be used to guide data collection strategy during collection. The 17sep21j and 17dec27a datasets had ice thickness measurements on average around 10–20 nm, whereas the 17nov21j ranged from 100–250 nm. Rabbit muscle aldolase, a 150 kDa homotetramer, has unit cell dimensions of 82.8 x 100.6 x 84.5 Å, so that individual particles are readily visible in ice 10–25 nm thick, but once embedded in ice that is 100–250 nm thick, contrast is much worse and individual particles are difficult to identify. In addition to the loss of contrast in the images, once the ice thickness is nearly 10 times that of the longest length of the particle of interest, it is likely that multiple layers of particles are present in the image, adhering to either side of the exposed air-water interface (Noble et al. 2017) which would also interfere with the possibility of getting a high resolution reconstruction.

We conclude that the most important factor in reaching a sub 3 Å map in less than 24 hours for our aldolase benchmark specimen is to have grids with ice thickness in the range of 10–20 nm. Use of a Cs-corrected system is not required for achieving these results as we have been able to replicate similar results using a well-aligned, non Cs-corrected systems. Similar results were achieved from the super-resolution and counting mode datasets, implying that it is not necessary to collect data in super-resolution mode to produce a sub 3 Å reconstruction. We also note that on-the-fly data processing, which includes frame alignment, CTF estimation, and particle picking, is critical to

Benchmarking cryo-EM single particle analysis workflow

214 maximizing the quantity and quality of data collected. Real-time feedback of the data helps guide the
 215 data collection strategy, allowing the user to be more critical about which regions of a grid, square,
 216 and hole to collect in (based on information on particle density, distribution, ice thickness, etc.), how
 217 long to pause between images (based on the motion correction plots), and how much defocus to
 218 apply (depending on how much contrast is visible in the aligned movies).

219 In summary, we show that with a commercially available protein and minimal biochemical
 220 purification, it is possible to prepare grids for characterizing microscopes at high resolution. While
 221 our protocol was tested on a Titan Krios microscope equipped with a K2 detector, this protocol could
 222 easily be adapted to other workflows (e.g. EPU or SerialEM) and microscope/detector combinations.
 223 Having a set of standard samples used by many EM labs will be generally useful for the field.

224 **Conflict of Interest**

225 The authors declare that the research was conducted in the absence of any commercial or financial
226 relationships that could be construed as a potential conflict of interest.

227 **Author Contributions**

228 LK, Performed sample preparation, microscope alignment, and data collection;; Wrote the
229 manuscript.

230 WR, Performed ice thickness measurements and analysis; Edited the manuscript.

231 EE, Performed data collection & image processing; Edited the manuscript.

232 MK, Performed microscope alignment and data collection; Edited the manuscript.

233 AC, Edited the manuscript.

234 AR, KJ, & DB, Performed sample preparation and data collection.

235 CP, Conceived and designed experiments; Edited the manuscript.

236 BC, Conceived and designed experiments; Edited the manuscript.

237 **Funding**

238 All work was performed at the Simons Electron Microscopy Center and National Resource for
239 Automated Molecular Microscopy located at the New York Structural Biology Center, supported by
240 grants from the Simons Foundation (SF349247), NYSTAR, and the NIH National Institute of
241 General Medical Sciences (GM103310) with additional support from Agouron Institute [Grant
242 Number: F00316] and NIH S10 OD019994-01.

243 **Acknowledgments**

244 The authors wish to thank Dr. Gabriel Lander (Scripps Research Institute) for helpful insight and
245 discussions.

246 **Data Availability Statement**

247 The datasets #1, 1a, 1b, 2, 2a, 2b, 3, 3a, &3b for this study can be found in the Electron Microscopy
248 Data Bank (EMDB) in the form of EM maps. Their accession codes are:

Sample #	Sample Name	EMDB
1	17sep21j – all images	7616
1a	17sep21j - < 25 nm ice thickness	7617
1b	17sep21j – 1 st 500 images	7614

Benchmarking cryo-EM single particle analysis workflow

2	17nov02c – all images	7551
2a	17nov02c – < 25 nm ice thickness	7562
2b	17nov02c – 1 st 700 images	7615
3	17dec27a – all images	7541
3a	17dec27a - < 25 nm ice thickness	7550
3b	17dec27a – 1 st 382 images	7528

249

250 References

- 251 Arnold, S. A., S. Albiez, A. Bieri, A. Syntychaki, R. Adaixo, R. A. McLeod, K. N. Goldie, H.
252 Stahlberg, and T. Braun. 2017. "Blotting-free and lossless cryo-electron microscopy grid
253 preparation from nanoliter-sized protein samples and single-cell extracts." *J Struct Biol* 197
254 (3):220-226. doi: 10.1016/j.jsb.2016.11.002.
- 255 Banerjee, S., A. Bartesaghi, A. Merk, P. Rao, S. L. Bulfer, Y. Yan, N. Green, B. Mroczkowski, R. J.
256 Neitz, P. Wipf, V. Falconieri, R. J. Deshaies, J. L. Milne, D. Huryn, M. Arkin, and S.
257 Subramaniam. 2016. "2.3 A resolution cryo-EM structure of human p97 and mechanism of
258 allosteric inhibition." *Science* 351 (6275):871-5. doi: 10.1126/science.aad7974.
- 259 Bartesaghi, A., A. Merk, S. Banerjee, D. Matthies, X. Wu, J. L. Milne, and S. Subramaniam. 2015.
260 "2.2 A resolution cryo-EM structure of beta-galactosidase in complex with a cell-permeant
261 inhibitor." *Science* 348 (6239):1147-51. doi: 10.1126/science.aab1576.
- 262 Campbell, M. G., B. M. Kearney, A. Cheng, C. S. Potter, J. E. Johnson, B. Carragher, and D.
263 Veessler. 2014. "Near-atomic resolution reconstructions using a mid-range electron
264 microscope operated at 200 kV." *J Struct Biol* 188 (2):183-7. doi: 10.1016/j.jsb.2014.09.008.
- 265 Campbell, M. G., D. Veessler, A. Cheng, C. S. Potter, and B. Carragher. 2015. "2.8 A resolution
266 reconstruction of the Thermoplasma acidophilum 20S proteasome using cryo-electron
267 microscopy." *Elife* 4. doi: 10.7554/eLife.06380.
- 268 Chen, S., G. McMullan, A. R. Faruqi, G. N. Murshudov, J. M. Short, S. H. Scheres, and R.
269 Henderson. 2013. "High-resolution noise substitution to measure overfitting and validate
270 resolution in 3D structure determination by single particle electron cryomicroscopy."
271 *Ultramicroscopy* 135:24-35. doi: 10.1016/j.ultramic.2013.06.004.
- 272 Cheng, Anchi, Edward T Eng, Lambertus Alink, William J. Rice, Kelsey D Jordan, Laura Y Kim,
273 Clinton S Potter, and Bridget Carragher. 2018. "High Resolution Single Particle Cryo-
274 Electron Microscopy using Beam-Image Shift." *bioRxiv*. doi: 10.1101/306241
- 275 Danev, R., and W. Baumeister. 2016. "Cryo-EM single particle analysis with the Volta phase plate."
276 *Elife* 5. doi: 10.7554/eLife.13046.

- 277 Danev, R., D. Tegunov, and W. Baumeister. 2017. "Using the Volta phase plate with defocus for
278 cryo-EM single particle analysis." *Elife* 6. doi: 10.7554/eLife.23006.
- 279 Henderson, R., A. Sali, M. L. Baker, B. Carragher, B. Devkota, K. H. Downing, E. H. Egelman, Z.
280 Feng, J. Frank, N. Grigorieff, W. Jiang, S. J. Ludtke, O. Medalia, P. A. Penczek, P. B.
281 Rosenthal, M. G. Rossmann, M. F. Schmid, G. F. Schroder, A. C. Steven, D. L. Stokes, J. D.
282 Westbrook, W. Wriggers, H. Yang, J. Young, H. M. Berman, W. Chiu, G. J. Kleywegt, and
283 C. L. Lawson. 2012. "Outcome of the first electron microscopy validation task force
284 meeting." In *Structure*, 205-14. United States: Copyright (c) 2012 Elsevier Ltd. All rights
285 reserved.
- 286 Herzik, M. A., Jr., M. Wu, and G. C. Lander. 2017. "Achieving better-than-3-A resolution by single-
287 particle cryo-EM at 200 keV." *Nat Methods* 14 (11):1075-1078. doi: 10.1038/nmeth.4461.
- 288 Kimanius, D., B. O. Forsberg, S. H. Scheres, and E. Lindahl. 2016. "Accelerated cryo-EM structure
289 determination with parallelisation using GPUs in RELION-2." *Elife* 5. doi:
290 10.7554/eLife.18722.
- 291 Lander, G. C., S. M. Stagg, N. R. Voss, A. Cheng, D. Fellmann, J. Pulokas, C. Yoshioka, C. Irving,
292 A. Mulder, P. W. Lau, D. Lyumkis, C. S. Potter, and B. Carragher. 2009. "Appion: an
293 integrated, database-driven pipeline to facilitate EM image processing." *J Struct Biol* 166
294 (1):95-102.
- 295 Li, X., P. Mooney, S. Zheng, C. R. Booth, M. B. Braunfeld, S. Gubbens, D. A. Agard, and Y. Cheng.
296 2013. "Electron counting and beam-induced motion correction enable near-atomic-resolution
297 single-particle cryo-EM." *Nat Methods* 10 (6):584-90. doi: 10.1038/nmeth.2472.
- 298 Merk, A., A. Bartesaghi, S. Banerjee, V. Falconieri, P. Rao, M. I. Davis, R. Pragani, M. B. Boxer, L.
299 A. Earl, J. L. S. Milne, and S. Subramaniam. 2016. "Breaking Cryo-EM Resolution Barriers
300 to Facilitate Drug Discovery." *Cell* 165 (7):1698-1707. doi: 10.1016/j.cell.2016.05.040.
- 301 Noble, Alex J, Venkata P Dandey, Hui Wei, Julia Brasch, Jillian Chase, Priyamvada Acharya, Yong
302 Zi Tan, Zhening Zhang, Laura Y Kim, Giovanna Scapin, Micah Rapp, Edward T Eng,
303 William J Rice, Anchi Cheng, Carl J Negro, Lawrence Shapiro, Peter D Kwong, David
304 Jeruzalmi, Amedee des Georges, Clinton S Potter, and Bridget Carragher. 2017. "Routine
305 Single Particle CryoEM Sample and Grid Characterization by Tomography." *bioRxiv*. doi:
306 10.1101/230276.
- 307 Punjani, A., J. L. Rubinstein, D. J. Fleet, and M. A. Brubaker. 2017. "cryoSPARC: algorithms for
308 rapid unsupervised cryo-EM structure determination." *Nat Methods* 14 (3):290-296. doi:
309 10.1038/nmeth.4169.
- 310 Rice, William J., Anchi Cheng, Alex J Noble, Edward T. Eng, Laura Y. Kim, Bridget Carragher, and
311 Clinton S. Potter. 2018. "Routine Determination of Ice Thickness for Cryo-EM Grids."
312 *bioRxiv*. doi: 10.1101/302018.
- 313 Rickgauer, J. P., N. Grigorieff, and W. Denk. 2017. "Single-protein detection in crowded molecular
314 environments in cryo-EM images." *Elife* 6. doi: 10.7554/eLife.25648.
- 315 Rohou, A., and N. Grigorieff. 2015. "CTFFIND4: Fast and accurate defocus estimation from electron
316 micrographs." *J Struct Biol* 192 (2):216-21. doi: 10.1016/j.jsb.2015.08.008.
- 317 Roseman, A. M. 2004. "FindEM--a fast, efficient program for automatic selection of particles from
318 electron micrographs." *J Struct Biol* 145 (1-2):91-9.

- 319 Russo, C. J., and L. A. Passmore. 2014. "Electron microscopy: Ultrastable gold substrates for
320 electron cryomicroscopy." *Science* 346 (6215):1377-80. doi: 10.1126/science.1259530.
- 321 Scheres, S. H., and S. Chen. 2012. "Prevention of overfitting in cryo-EM structure determination." In
322 *Nat Methods*, 853-4. United States.
- 323 Suloway, C., J. Pulokas, D. Fellmann, A. Cheng, F. Guerra, J. Quispe, S. Stagg, C. S. Potter, and B.
324 Carragher. 2005. "Automated molecular microscopy: the new Legimon system." *J Struct Biol*
325 151 (1):41-60. doi: 10.1016/j.jsb.2005.03.010.
- 326 Zheng, S. Q., E. Palovcak, J. P. Armache, K. A. Verba, Y. Cheng, and D. A. Agard. 2017.
327 "MotionCor2: anisotropic correction of beam-induced motion for improved cryo-electron
328 microscopy." *Nat Methods* 14 (4):331-332. doi: 10.1038/nmeth.4193.

329

Table 1. Data collection statistics

All datasets were collected on the same Titan Krios equipped with an energy filter and spherical aberration corrector at 300 keV accelerating voltage. Micrographs were collected on the K2 Summit DED, at either counting or super-resolution mode, at a nominal magnification of 130,000x, equivalent to a 0.85 Å pixel size at a dose rate of 8.0 e⁻/pixel/sec. Images were targeted by image shift movement, with a nominal defocus range of -1.0 to -2.0 µm underfocus. The difference in the number of micrographs collected per hour for the 17nov02c and 17dec27a is due to the delayed start of early return on the K2 camera system, which is used to speed up exposure acquisition speeds by outputting only the first few frames of a movie instead of the entire movie so that the camera can continuously collect images.

	17sep21j	17nov02c	17dec27a
Counting vs Super-resolution	counting	super-resolution	super-resolution
Exposure time (ms)	6600	6000	6000
Total dose (e⁻/Å²)	68	63	63
Duration of data collection	18 hours	52 hours	40 hours
Micrographs collected (per hour)	~38	~31	~40
# images total	699	1635	1614

Table 2. Processing and Reconstruction statistics

Datasets were sorted based on three methods, using all micrographs, using micrographs with < 25 nm ice thickness and using only the first few hundred micrographs. This is to test whether it is more important to collect and process data based on the quantity of data (all micrographs), quality of data (< 25 nm ice thickness), or time spent on data collection and processing (first few hundred micrographs). All 2D and 3D processing was performed using Cryosparc.

	17sep21j	17sep21j	17sep21j	17nov02c	17nov02c	17nov02c	17dec27a	17dec27a	17dec27a
Sorting method	All img	< 25 nm ice thickness	1 st 500 img	All img	< 25 nm ice thickness	1 st 700 img	All img	< 25 nm ice thickness	1 st 382 img
Dataset number	#1	#1a	#1b	#2	#2a	#2b	#3	#3a	#3b
Duration of data collection	18.0 hours	18.0 hours	13.5 hours	52.0 hours	52.0 hours	24.0 hours	40.0 hours	40.0 hours	10.0 hours
# images total	699	699	699	1635	1635	1635	1614	1614	1614
# images used	699	535	500	1635	63	700	1614	1108	382
# picks	642K	491K	256K	1,380K	60K	685K	1,214K	975K	234K
Duration of 2D classification	0.8 hours	0.4 hours	0.3 hours	1.3 hours	0.3 hours	0.4 hours	1.1 hours	1.1 hours	0.4 hours
# particles after 2D	373K	374K	133K	464K	26K	198K	498,000	369K	87K
% particles after 2D	58%	76%	52%	34%	43%	29%	41%	38%	37%
Duration of 3D classification	1.2 hours	1.7 hours	0.9 hours	3.9 hours	0.5 hours	0.5 hours	6.3 hours	5.1 hours	0.8 hours
# particles into refinement	219K	124K	62K	204K	22K	75K	205K	187K	87K
% particles into refinement	59%	33%	47%	44%	85%	38%	41%	52%	100%
Duration of refinement	0.9 hours	0.9 hours	0.9 hours	1.9 hours	0.5 hours	0.5 hours	1.5 hours	1.4 hours	0.7 hours
Ice thickness range	10 – 20 nm	10 – 20 nm	10 – 20 nm	100 – 250 nm	100 – 250 nm	100 – 250 nm	10 – 20 nm	10 – 20 nm	10 – 20 nm
Total processing time	2.9 hours	3.0 hours	2.0 hours	7.1 hours	1.2 hours	1.4 hours	8.9 hours	7.6 hours	1.9 hours
Resolution (global)	2.5 Å	2.5 Å	2.8 Å	3.0 Å	3.5 Å	4.6 Å	2.4 Å	2.4 Å	2.8 Å

Table 3. Ranking of datasets based on data collection and processing time and resolution.

Datasets were ranked primarily on total data collection + processing time and secondarily on nominal resolution. Six out of nine datasets went to $< 3 \text{ \AA}$. We find that all $< 3 \text{ \AA}$ reconstructions come from datasets with 10 – 20 nm ice thickness and that more than half of those $< 3 \text{ \AA}$ datasets were acquired in under 24 hours. Datasets that do not go $< 3 \text{ \AA}$ had ice thickness measurements ranging from 100 – 250 nm.

Ranking	Dataset	Total collection + processing time	resolution	# particles	Ice thickness range
1	#3b	11.9 hours	2.8 \AA	87K	10 – 20 nm
2	#1b	15.5 hours	2.8 \AA	62k	10 – 20 nm
3	#1	20.9 hours	2.5 \AA	219k	10 – 20 nm
4	#1a	21.0 hours	2.5 \AA	124k	10 – 20 nm
5	#3a	47.6 hours	2.4 \AA	186k	10 – 20 nm
6	#3	48.9 hours	2.4 \AA	205k	10 – 20 nm
7	#2	59.1 hours	3.0 \AA	204k	100 – 250 nm
8	#2a	53.2 hours	3.5 \AA	22k	100 – 250 nm
9	#2b	25.4 hours	4.6 \AA	75K	100 – 250 nm

Figure 1. Comparing images from thick versus thin ice.

Exemplary images from (a) 17sep21j (#1), (e) 17nov02c (#2), and (i) 17dec27a (#3) datasets. Quantitative metrics such as the estimation of resolution from CTFFindV4 (b, f, & j) and qualitative metrics such as the presence/absence of the water diffraction ring around the 3 Å mark (c, g, & k), and ice thickness measurements of the micrographs (d, h, & l), should be monitored during data collection. A CTFFindV4 resolution estimation worse than 4 Å and the presence of a strong water diffraction ring are both indicative of thick ice, and areas like this should be avoided. All images were acquired with ~1.5 μm defocus. Ice thickness measurements provide a useful metric for data quality (d, h, & l). Datasets 17sep21j and 17dec27a both contain a majority of images where ice thickness is in the range 0 – 20 nm. The majority of 17nov02c images have thickness in the range 0 – 10 nm thickness (ice that is too thin or completely absent) or very thick ice in the range 100 – 250 nm. The dimensions of aldolase are ~100 Å so this thick ice is more than 20 times more than the longest dimension of the particle.

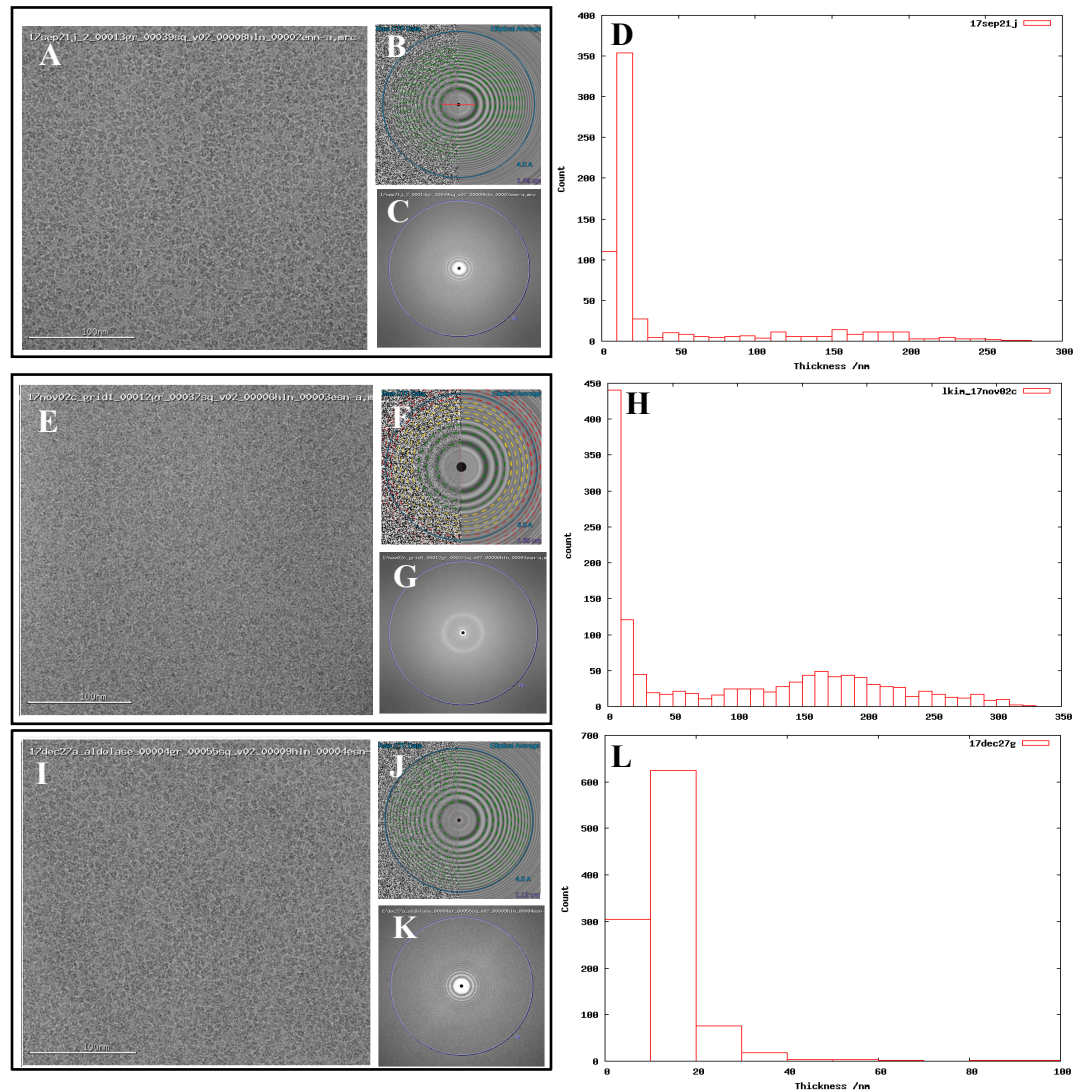


Figure 2. Comparing 3D reconstructions from thick versus thin ice

2D and 3D processing results from 17sep21j (dataset #1) and 17nov02c (dataset #2) which yielded maps at 2.5 Å and 3.0 Å resolution, respectively. Dataset #1 has thinner ice in the raw micrographs, ranging from 10 – 20 nm thick, whereas dataset #2 has thicker ice, ranging from 100 – 250 nm thick. A raw micrograph (a & g), 2D classification (b & h), FSC plot (c & i), sphericity (d & j), 3D map (e & k) and local resolution map (f & l). Both datasets have about 200,000 particles contributing to the final refinement but dataset #1 is both qualitatively and quantitatively better than dataset #2.

